

# Topological nodal line in $\text{ZrTe}_2$ demonstrated by nuclear magnetic resonance

Yefan Tian, Nader Ghassemi, and Joseph H. Ross, Jr.\*

Department of Physics and Astronomy, Texas A&M University, College Station, TX 77843, USA

(Dated: September 15, 2020)

In this work, we report nuclear magnetic resonance (NMR) combined with density functional theory (DFT) studies of the transition metal dichalcogenide  $\text{ZrTe}_2$ . The measured NMR shift anisotropy reveals a quasi-2D behavior connected to a topological nodal line close to the Fermi level. With the magnetic field perpendicular to the  $\text{ZrTe}_2$  layers, the measured shift can be well-fitted by a combination of enhanced diamagnetism and spin shift due to high mobility Dirac electrons. The spin-lattice relaxation rates with external field both parallel and perpendicular to the layers at low temperatures match the expected behavior associated with extended orbital hyperfine interaction due to quasi-2D Dirac carriers. In addition, calculated band structures also show clear evidence for the existence of nodal line in  $\text{ZrTe}_2$  between  $\Gamma$  and  $A$ . For intermediate temperatures, there is a sharp reduction in spin-lattice relaxation rate which can be explained as due to a reduced lifetime for these carriers, which matches the reported large change in mobility in the same temperature range. Above 200 K, the local orbital contribution starts to dominate in an orbital relaxation mechanism revealing the mixture of atomic functions.

## I. INTRODUCTION

In recent years, there has been great interest in layered transition metal dichalcogenides (TMDCs), comprised of a wide range of transition metal (Mo, W, Ta, Zr, Hf, etc.) and chalcogen (S, Se, or Te) elements. The TMDC family offers platforms for exploring striking physical phenomena and exotic electronic device applications [1]. Among TMDCs,  $\text{ZrTe}_2$  has been relatively little investigated; however, recent work [2–4] has indicated interesting topological features in this material both in the normal state and as a doped superconductor. Also, other zirconium tellurides have been of considerable interest. For instance,  $\text{ZrTe}_5$  shows interesting topological properties and unique physical properties such as chiral magnetic effect [5] and three-dimensional quantum Hall effect [6].  $\text{ZrTe}_5$  also exhibits a topological phase transition separating the strong and weak topological insulator states [7–9] with a temperature-driven valence and conduction band inversion associated with this topological phase transition [7]. The layered material  $\text{ZrTe}_3$  has also been long studied due to interesting behavior such as a charge density wave phase transition [10]. Recently, theoretical calculations indicate distinctive topological behavior in  $\text{ZrTe}$ , which possesses triple-point fermions coming from the three-fold degenerate crossing points formed by the crossing of a double-degeneracy band and a nondegeneracy band [11].

Regarding  $\text{ZrTe}_2$ , the theoretical predictions from several groups give rather different results [2–4, 12–14], leading to the importance of determining its topological nature. Although several theoretical reports [2, 12] predicted  $\text{ZrTe}_2$  to be a simple metal, there is no direct experimental evidence supporting this result. However, recent ARPES studies [4] present evidence of massless

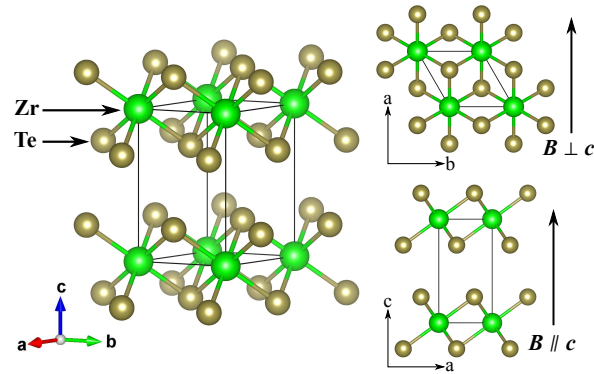


FIG. 1. Crystal structure of 1T- $\text{ZrTe}_2$  with P-3m1 space group, showing van der Waals-bonded layered structure.

Dirac fermions observed in the  $\text{ZrTe}_2$  bulk phase, while the DFT calculations [3, 4] also support the topological semimetal prediction. As a topological semimetal candidate from the layered TMDC family,  $\text{ZrTe}_2$  may show attractive electrical transport phenomena and promising prospects for quantum device applications.

In this work, we have studied  $\text{ZrTe}_2$  using NMR techniques combined with DFT computations, revealing its topological nature and electronic properties as a quasi-2D topological dichalcogenide. Shifts and spin-lattice relaxation rates for both  $B \parallel c$  and  $B \perp c$  orientations have been measured, which show that the layered dichalcogenide  $\text{ZrTe}_2$  presents Dirac quasi-2D features associated with a nodal line extending in the direction perpendicular to the layers.

## II. EXPERIMENTAL AND COMPUTATIONAL METHODS

The  $\text{ZrTe}_2$  single crystals (crystal structure shown in Fig. 1) were prepared using chemical vapor transport

\* [jhross@tamu.edu](mailto:jhross@tamu.edu)

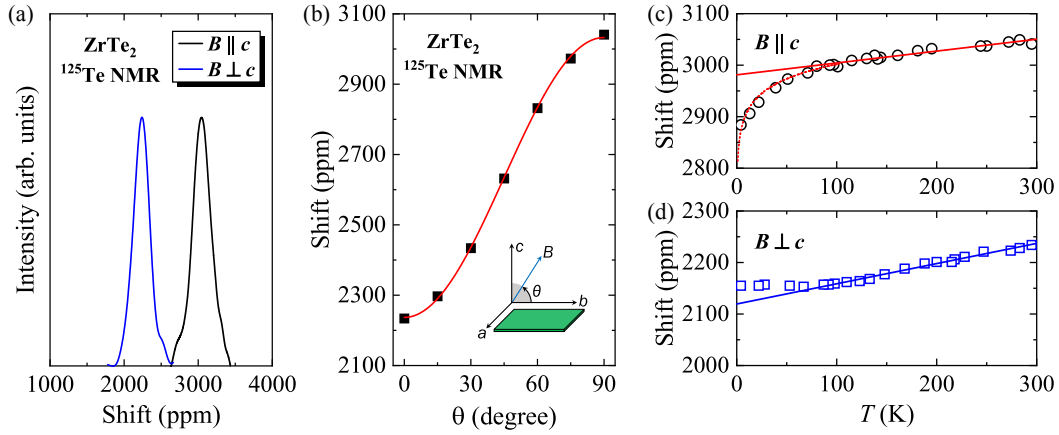


FIG. 2. (a)  $^{125}\text{Te}$  lineshapes of  $\text{ZrTe}_2$  at room temperature. (b) Angular dependence of shift at room temperature. The red solid curve is a fit to Eq. (1). Shift vs temperature for (c)  $B \parallel c$  (magnetic field perpendicular to the layers) with linear and  $\ln(T)$  curves as guides to the eye and (d)  $B \perp c$  (magnetic field parallel to the layers).

method. The stoichiometric mixture of Zr and Te powder was sealed in a quartz tube with iodine being used as transport agent (2 mg/cm<sup>3</sup>). Plate-like single crystals with metallic luster were obtained via the vapor transport growth with a temperature gradient from 950 °C to 850 °C. Cameca SXFive microprobe measurements indicate a uniform phase  $\text{Zr}_{0.99}\text{Te}_2$ .

NMR experiments utilized a custom-built spectrometer at a fixed field  $B \approx 9$  T. Many individual crystals were stacked with the  $c$  axes aligned and the sample was measured with the field parallel to  $c$  ( $B \parallel c$ ) and in the basal plane ( $B \perp c$ ). The  $a$  axis orientation was not identified for these crystals.  $^{125}\text{Te}$  shifts were calibrated by aqueous  $\text{Te}(\text{OH})_6$  and adjusted for its  $\delta = 707$  ppm paramagnetic shift to the dimethyltelluride standard [15].

The band structure and density of states calculations were carried out in the framework of the density functional theory (DFT) by employing the APW plus local orbital (APW+lo) method [16] with the PBE potential [17] as implemented in the WIEN2K code [18]. A mesh of 1000  $k$ -points was employed in the irreducible wedge of the hexagonal Brillouin zone [see Fig. 4(d)] corresponding to the grids of  $10 \times 10 \times 10$  in the Monkhorst-Pack [19] scheme. The cutoff parameter of  $k_{\text{max}} = 7/R_{\text{MT}}$  inside the interstitial region was used for the expansions of the wave functions in terms of the plane waves.

### III. EXPERIMENTAL AND COMPUTATIONAL RESULTS

#### A. Shift

Consistent with the single local environment for Te in the 1T- $\text{ZrTe}_2$  structure, there is only one peak observed in the  $^{125}\text{Te}$  spectra as shown in Fig. 2(a). The angular dependence of the NMR shift (with  $\theta$  defined between the  $ab$  layer and the magnetic field  $B$ ) is shown

in Fig. 2(b). The room-temperature shift was fitted [red curve in Fig. 2(b)] to

$$K = K_{\text{iso}} + \frac{3 \cos^2 \theta - 1}{2} \cdot \Delta K, \quad (1)$$

where  $K_{\text{iso}} = 2767 \pm 3$  ppm is the isotropic shift and  $\Delta K = -530 \pm 4$  ppm. By symmetry, the shift will not depend on orientation in the basal plane, which is confirmed by the absence of additional inhomogeneous line broadening for this orientation [Fig. 2(a)]. Ref. [20] gives  $\delta_{\text{iso}} = 1825$  ppm with  $\text{Te}(\text{OH})_6$  as reference, which corresponds to 2532 ppm, a similar shift as reported here, considering the large width measured in Ref. [20].

Figs. 2(c) and 2(d) show the temperature dependence of the  $^{125}\text{Te}$  shift for  $B \parallel c$  and  $B \perp c$  ( $K_{\parallel c}$  and  $K_{\perp c}$ ), respectively. The shifts were obtained by identifying the highest intensity position of the measured single-peak  $^{125}\text{Te}$  spectra. The  $K_{\parallel c}$  results decrease monotonically vs  $T$ , with a sharp decrease as  $T$  approaches zero. A detailed analysis will be discussed below. For  $K_{\perp c}$ , there is a clear change at  $\sim 50$  K in the shift vs  $T$ . Above 50 K, the shift appears to be linearly dependent on temperature, with a small positive slope. Below 50 K, the shift is nearly temperature independent. These results are indicative of quasi-2D Dirac-node behavior with detailed discussion below. The carrier concentration shown in Ref. [4] is in the order of  $10^{19}$  cm<sup>-3</sup>, which presents the fact that the large measured shifts are mostly chemical shifts due to electronic states away from the Fermi energy ( $\varepsilon_F$ ); however, the temperature-dependence is dominated by Knight shifts due to carriers at  $\varepsilon_F$ , and for convenience we label observed shift, which is the sum of these shift terms, as  $K$ .

#### B. Spin-lattice relaxation

Spin-lattice relaxation results, measured by inversion recovery, could be well fitted to a single exponential

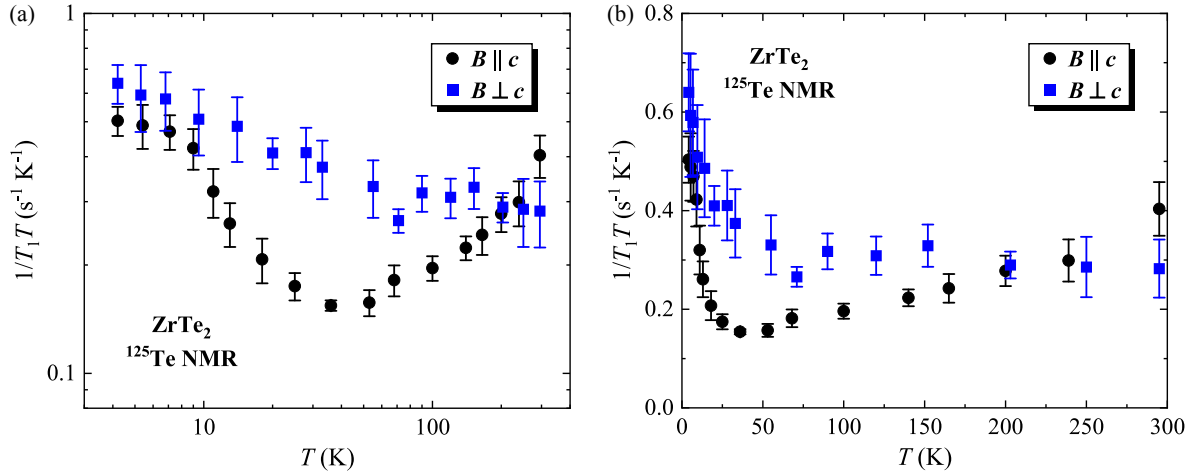


FIG. 3.  $1/T_1T$  vs  $T$  for both orientations  $B \parallel c$  (perpendicular to the layers) and  $B \perp c$  (parallel to the layers) in (a) log scale and (b) linear scale.

$M(t) = (1 - Ce^{-t/T_1})M(\infty)$ , giving  $1/T_1T$  values shown in Figs. 3(a) and 3(b). The results decrease rapidly at low temperatures as  $T$  increases, especially  $(1/T_1T)_{\parallel c}$ , which exhibits a sudden drop-off above about 10 K. Near 50 K, which is also the temperature at which  $K_{\perp c}$  exhibits a change in behavior, the relaxation results also exhibit a characteristic change, with  $1/T_1T$  leveling off, and  $1/T_1T$  exhibiting a minimum near 40 K and then steadily increasing. In metals,  $1/T_1T$  is often dominated by  $s$ -electron Fermi contact and proportional to  $g^2(\varepsilon_F)$ . However, as shown below, similarly to  $\text{ZrTe}_5$  [21] Dirac state in  $\text{ZrTe}_2$  is also dominated by Te  $p$  states, which produce a dominant orbital contribution to  $1/T_1T$ , with the largest term due to the high-mobility Dirac carriers.

### C. DFT computations

From reports by several groups [2–4, 12–14], there have been some conflicts about the topological nature of  $\text{ZrTe}_2$  as detected in DFT results. Ref. [14] suggests a semimetallic state of  $\text{ZrTe}_2$  without any topological nature. Ref. [4] suggests  $\text{ZrTe}_2$  is a topological semimetal, consistent with its ARPES results. Both Refs. [3, 4] indicate a Dirac point at  $\Gamma$  with the Dirac node close to the chemical potential and an electron pocket at  $M$  in the conduction band. The lattice parameters used in Ref. [4] are about 1–2% expanded from experimental values. However, these parameters were obtained from a DFT energy optimization, and they provided an approximate match for the reported ARPES results, with the distinction that the calculated Dirac node is roughly 0.5 eV higher in energy than observed, and the calculations point to much larger overlaps at  $\varepsilon_F$  of the normal-electron pockets at the  $L$  and  $M$  points than what is observed. Ref. [14] included a correction for the van der Waals interaction, leading to a much smaller overlap at the  $L$  and  $M$  points; however, a large gap opened throughout the Brillouin zone, in seeming contradiction with magnetotransport results [22] as well as APRES results quoted above. It is likely that the well-known difficulty in predicting band energies near the gap in standard GGA functionals such as PBE is responsible for the discrepancies between the calculated results and the observations. For further investigation we used the lattice parameters of Ref. [4] ( $a = 3.909 \text{ \AA}$  and  $c = 6.749 \text{ \AA}$ ) for DFT calculations, with the understanding that the energies likely include an offset near  $\varepsilon_F$ .

Results of the DFT calculations, with spin-orbit coupling included, are shown in Figs. 4(a)–(c). The nearly-dispersionless band from  $\Gamma$  to  $A$  connects to Dirac-like features at  $\Gamma$  (as previously identified [3, 4]) and also at  $A$ , and this band is doubly degenerate except for a gap of about 20 meV very close to  $\Gamma$ , identified [4] as associated with a band inversion. The mapping in reciprocal space, and a schematic of the nodal line between  $\Gamma$  and  $A$ , are demonstrated in Figs. 4(d) and 4(e). Also note that the partial DOS results show that Te  $p$  orbitals mostly locate at these Dirac bands away from the node while Zr  $d$  orbitals dominate at the node itself, and the Zr orbitals dominate the electron-type pockets at  $L$  and  $M$ . There is also a separate high-dispersion band crossing  $\Gamma$  just below the node energy.

As an estimate of the Fermi velocity for the Dirac nodal line, we analyzed the linear slope in the  $\Gamma$ - $M$  and  $A$ - $L$  directions leading up to the nodal line according to  $\varepsilon = \hbar v_F k$ , and obtained  $0.69$  and  $0.65 \times 10^6 \text{ m/s}$ . Based on these values, we used the mean value of  $0.67 \times 10^6 \text{ m/s}$ , which is a typical value for Dirac semimetals [23] for numerical estimates below. A similar value was estimated for the monolayer case [3]. The extra pockets at  $L$  and  $M$  contain ordinary electrons, and the existence of both Dirac and ordinary electrons at  $\varepsilon_F$  leads to additional complexity in this case, although experimental indications [3, 4] point to a much smaller overlap between the  $M$  pocket and the Dirac valence band

As an estimate of the Fermi velocity for the Dirac nodal line, we analyzed the linear slope in the  $\Gamma$ - $M$  and  $A$ - $L$  directions leading up to the nodal line according to  $\varepsilon = \hbar v_F k$ , and obtained  $0.69$  and  $0.65 \times 10^6 \text{ m/s}$ . Based on these values, we used the mean value of  $0.67 \times 10^6 \text{ m/s}$ , which is a typical value for Dirac semimetals [23] for numerical estimates below. A similar value was estimated for the monolayer case [3]. The extra pockets at  $L$  and  $M$  contain ordinary electrons, and the existence of both Dirac and ordinary electrons at  $\varepsilon_F$  leads to additional complexity in this case, although experimental indications [3, 4] point to a much smaller overlap between the  $M$  pocket and the Dirac valence band

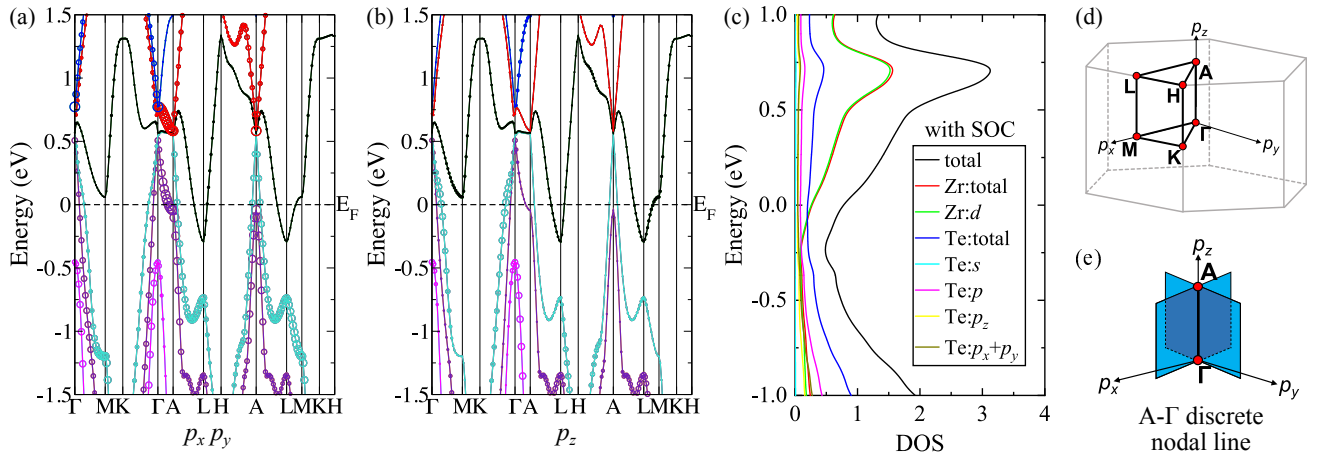


FIG. 4. Band structures of  $\text{ZrTe}_2$  with spin-orbit coupling, with superposed circles showing weights for (a)  $p_x + p_y$  and (b)  $p_z$  Te orbitals. The circle size represents the partial state density of Te. (c) Density of states for  $\text{ZrTe}_2$ . (d) 3D view of the hexagonal Brillouin zone with high-symmetry points. (e) Sketch of discrete nodal line between  $\Gamma$  and A.

than what is calculated. With the  $\sqrt{\varepsilon}$  type density of states near  $\varepsilon_F$  dominated by the M pocket we fitted to  $g(\varepsilon) = \sqrt{(2\varepsilon(m^*)^3)/(\pi^2\hbar^3)}$  and obtained an estimate of  $m^* = 1.7m_e$  for this pocket. In the model discussed below, the position of Fermi level is near the edge of this pocket, and very close to the nodal line.

#### IV. DISCUSSION AND ANALYSIS

##### A. Knight shift

As shown in Figs. 2(c) and 2(d), there is an obvious difference between the measured shifts of  $B \parallel c$  and  $B \perp c$  orientations, especially at low temperatures. The observed low- $T$  divergence for  $K_{\parallel c}$  follows approximately a  $\ln(T)$  curve, characteristic of the divergent orbital susceptibility for Dirac semimetals [24, 25], although the absence of the corresponding behavior for  $K_{\perp c}$  points to a quasi-2D Dirac semimetal rather than 3D point-node behavior.

To analyze this situation, first we note that the shifts will be largely due to the dominant  $p$ -electrons for Te in  $\text{ZrTe}_2$ , contributing a combination of core polarization and spin-dipolar shifts, which are electron spin mechanisms, as well as orbital shifts, with the latter likely dominated by the large bulk orbital response of the Dirac electrons rather than due to local orbitals. The core polarization mechanism normally contributes an isotropic shift (the same sign for both orientations) and the spin-dipolar, anisotropic shift [second term in Eq. (1)]. However, the vanishing divergent behavior for  $B \perp c$  points to a different physical mechanism for the two orientations rather than shift anisotropy, and thus, we analyze the  $B \parallel c$  divergence in terms of the spin response of quasi-2D Dirac electrons due to the separation of Landau levels with  $B \parallel c$ , plus an orbital shift dominated by quasi-2D

orbital currents confined to the basal plane.

For quantitative comparison, first we consider the case of a 3D point node. The Knight shift due to the orbital interaction in a 3D massless Dirac electron case can be expressed as [25],

$$K = K_0 - \frac{1}{6\pi^2} \frac{\mu_0 v_F e^2}{\hbar} \ln \left( \frac{W}{k_B T} \right), \quad (2)$$

where  $K_0$  is a  $T$ -independent term and  $W$  is a bandwidth cutoff. Note this is the low field case. For  $v_F$ , we used  $v_F = 6.7 \times 10^5$  m/s as described above. With this prefactor, we obtain from Eq. (2) a difference in shift of 4 ppm between the temperatures 10 K and 100 K. However, in addition, since this mechanism is heavily linked to demagnetizing effect, the corresponding demagnetizing field should also be considered. The overall sample size (around  $2 \times 2 \times 0.5$  mm $^3$ ) implies a demagnetizing factor of approximately 5 for such a bulk-susceptibility contribution for the  $B \parallel c$  orientation. Thus, this mechanism is expected to lead to a difference in shift of less than 1 ppm over this temperature range, much less than what is observed.

As alternative we consider the effects of diamagnetic currents due to Dirac nodal line charge carriers, for a node line oriented along the  $c$  direction. In this case, with currents confined to the basal plane, the diamagnetic response is equivalent to that of a 2D Dirac gas, and we can follow the treatment used for the case of graphene [26]. Also note that the effect vanishes for  $B \perp c$ , due to the absence of high mobility circulating currents perpendicular to the plane. Thus, for  $\text{ZrTe}_2$  we modeled this system as including a quasi-2D Dirac line, with the addition of an electron pocket of normal electrons crossing the node energy ( $\varepsilon_{\text{node}}$ ), as indicated by DFT calculations and by ARPES measurements [4]. For the normal electron pocket we assumed an effective mass  $m^*/m_e = 1$ , close to the value we estimated for the pocket at the M

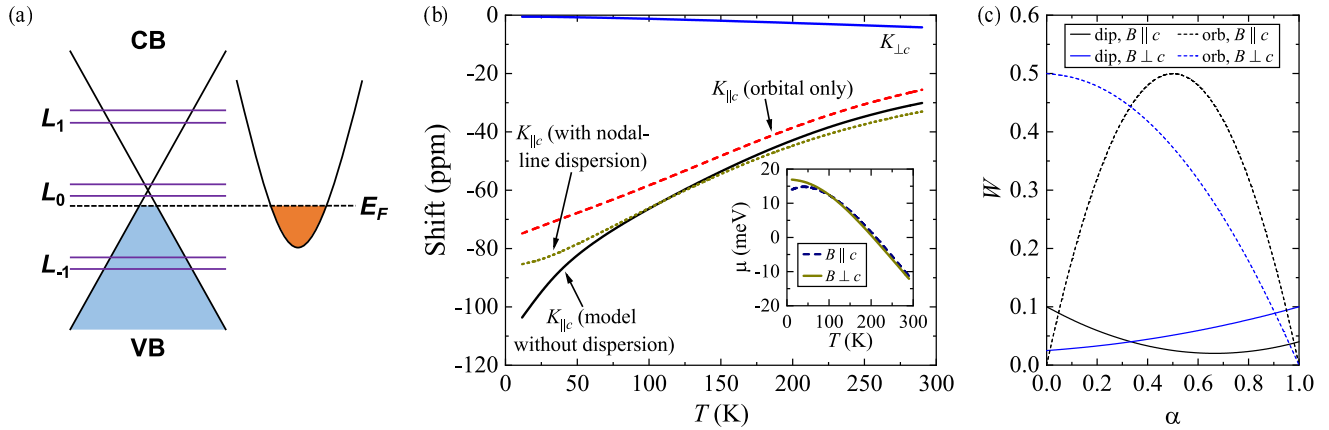


FIG. 5. (a) Sketch of Dirac band and electron pocket. (b) Simulated shifts for both orientations. Inset: chemical potential vs  $T$ . (c)  $W = 1/2T_1$  is the dipolar and orbital relaxation rates divided by  $2\pi(\gamma_e\gamma_n\hbar^{3/2})^2g^2(\varepsilon_F)k_BT\langle r^{-3} \rangle^2$ .  $\alpha$  is the mixture of orbitals ( $p_x + p_y$ ) vs  $p_z$ .

point in DFT calculations (above). Also similar to the description above for 3D Dirac electrons, we assumed  $v_{\perp} = 6.7 \times 10^5$  m/s, for which in the 9 T NMR field applied perpendicular to the layers, this gives Landau-level energies  $\varepsilon_{LL}(N) = \pm\sqrt{(2e\hbar v_{\perp}^2 B|N|)} = \pm73\sqrt{(|N|)}$  meV, and a volume density of carriers per spin level  $n_{LL} = B/(\Phi_0 c) = 3.3 \times 10^{18}$  cm $^{-3}$ , where  $\Phi_0 = 4.14 \times 10^{-15}$  T m $^2$ . The gyromagnetic ratio is not known for these carriers, so we assumed  $g = 2$ . As was estimated from ARPES results [4] we assumed that a fixed density of carriers  $n_{\text{total}} = 10^{19}$  cm $^{-3}$  is divided between these band features. Thus, to solve for the chemical potential we specified,

$$n_{\text{total}} = \int_0^{\infty} f(\varepsilon, \mu) g_{CB}(\varepsilon) d\varepsilon + \sum_{s=-1/2}^{1/2} \sum_{N=-N_0}^{N_0} n_{LL} f(\varepsilon_N, \mu) - n_{LL} - \sum_{s=-1/2}^{1/2} \sum_{N=-N_0}^{-1} n_{LL}, \quad (3)$$

where  $g_{CB}(\varepsilon) = \sqrt{(2\varepsilon m^*{}^3)/(\pi^2\hbar^3)}$  is the density of states in the normal-carrier pocket with its minimum set to  $\varepsilon = 0$ ,  $\varepsilon_N = \varepsilon_{\text{node}} + \mu_B g B s + \varepsilon_{LL}(N)$  represents the Landau level energies,  $f(\varepsilon, \mu) = 1/[1 + e^{(\varepsilon - \mu)/k_B T}]$  is the Fermi function, and  $N_0$  is a cutoff for the sum. To model the  $B \perp c$  case for which the Landau levels collapse, we replaced the sum over Landau levels in Eq. (3) with an integral over the 2D Dirac density of states  $g_D(\varepsilon) = |\varepsilon - \varepsilon_{\text{node}} \pm \mu_B g B s|/[\pi c(\hbar v_{\perp})^2]$  per spin, also similarly normalized for hole and electron states. Solving numerically for  $\mu(T)$ , we obtained the results shown in the inset of Fig. 5(b), solved for the case  $\varepsilon_{\text{node}} = 12$  meV. Because of the significant carrier density  $n_{LL}$  at each Landau level energy including  $N = 0$ , the  $B \parallel c$  field tends to pull  $\mu$  into  $\varepsilon_{\text{node}}$  at low temperature [27], as can be seen from the results shown in the inset of Fig. 5(b). Recently anomalous magnetotransport effects

were also identified in a layered Dirac material due to field-induced alignment of the chemical potential [28].

The diamagnetic susceptibility is  $\chi = \mu_0 \partial M / \partial B$ , and we calculated [26] the magnetization for  $B \parallel c$  as  $M = -(1/V) \partial \Omega / \partial B$  with the grand potential volume density given by

$$\Omega/V = -k_B T n_{LL} \sum_{N=-m}^m \ln[1 + e^{(\varepsilon_N - \mu)/k_B T}], \quad (4)$$

with  $m$  a numerical cutoff for the sum. For numerical calculation of the  $B$  derivative, we adopted the method described in Ref. [26] to normalize for the  $B$ -dependence caused by the numerical cutoff  $m$ . Using the  $\mu(T)$  results obtained as described above, we thus arrived at an estimation of  $\chi$  for the  $B \parallel c$  case. As noted above, we also estimated a demagnetization factor of 80% for our sample for  $B \parallel c$ , and thus multiplying  $\chi$  by 1/5 we arrived at an estimated bulk-diamagnetic contribution to  $K_{\parallel c}$  shown by the dashed curve in the main plot of Fig. 5(b). Note that in the  $B$ -derivative of  $\Omega/V$  we included changes in  $n_{LL}$  and  $\varepsilon_{LL}(N)$ , but not in the numerical solutions  $\mu(T)$ . The difference should be small, since for most of the temperature range the CB pocket determines the position of  $\mu$ , while at low temperatures the results have the linear- $T$  behavior equivalent to the case that  $\mu$  is fixed at  $\varepsilon_{\text{node}}$  [26], due to the pulling effect of the magnetic field discussed above. To calculate the spin contribution to the shift, we first calculated the Dirac-electron spin density as

$$n_{\text{spin}} = \sum_{s=-1/2}^{1/2} (-1^{2s}) \sum_{N=-N_0}^{N_0} n_{LL} f(\varepsilon_N, \mu) \quad (5)$$

both for  $B \parallel c$  and  $B \perp c$  using the corresponding  $\mu(T)$  values obtained above. Assuming the core-polarization hyperfine contribution dominates for the Te  $p$ -electrons participating in the Dirac node, we used the estimated

[29] hyperfine field  $B_{\text{cp}}^{\text{HF}} = -15$  T in calculating the spin shift as  $K_{\text{spin}} = n_{\text{spin}}(B_{\text{cp}}^{\text{HF}}/9 \text{ T})(V_{\text{cell}}/2)$ , with 9 T the applied NMR field and the sample volume per Te atom given by  $V_{\text{cell}}/2 = 50 \text{ \AA}^3$ . The results were added to the calculated  $T$ -dependent diamagnetic orbital shift, giving the spin+orbital result plotted in Fig. 5(b) (lowest curve). The results are comparable to the observed shift behavior and have the same general temperature dependence. Since there is considerable likelihood that  $g$  differs from 2 [30–33], we did not attempt a quantitative fitting; however, it appears that this model correctly captures the low- $T$  behavior, and that a combination of spin susceptibility and orbital diamagnetism, both strongly enhanced in the quantum limit for the  $B \parallel c$  orientation, are responsible for the observations.

Note that in the DFT results (Fig. 4), a small dispersion appears in the nodal line, with the changes covering a range of approximately 20 meV between  $\Gamma$  and A. To model the effect of this behavior, we added a simple linear dispersion to the  $\varepsilon_{\text{node}}$  position. This was done by modifying the sum over Landau level numbers  $N$  in Eqs. (3)–(5), replacing the summands having fixed  $\varepsilon_{\text{node}}$  by an integrated square distribution covering a range  $\varepsilon_{\text{node}} \pm 10$  meV, and repeating the numerical calculations described above with otherwise identical parameters. This yielded the spin+orbital shift result shown in the dotted curve in Fig. 5(b): the main effect is a softening of the spin contribution as  $T$  approaches zero; however, the calculated magnitude is similar to that of the completely dispersionless case.

## B. Relaxation mechanisms

The low- $T$   $1/T_1$  results exhibit an anisotropy and temperature dependence which does not match the corresponding behavior of the measured shifts. Thus, we expect the  $T_1$  behavior is not a result of a Korringa-type spin contribution [34]. On the other hand, the orbital shift and  $T_1$  are not governed by a Korringa relation [24], and the behavior in the low- $T$  limit matches what is predicted for the quasi-2D orbital case due to high-mobility carriers. For the quasi-2D free-electron gas (i.e., metallic layers where electrons in each layer behave as a 2D free-electron gas), Lee and Nagaosa obtained the relaxation rates due to the orbital interaction when the magnetic field is applied parallel and perpendicular to the layers [35], which corresponds to a ratio between  $(1/T_1T)_{\parallel c}$  and  $(1/T_1T)_{\perp c}$  of 2 : 3. As shown in Fig. 3, excluding a  $T$ -independent background, the low- $T$   $(1/T_1T)_{\parallel c}$  and  $(1/T_1T)_{\perp c}$  reaches a ratio close to 2 : 3. Thus, the low- $T$  behavior can be modeled as below using the extended orbital scenario. For the quasi-2D Dirac electron system,

the orbital contribution can be expressed as [25]

$$\left( \frac{1}{T_1T} \right)_{\perp c} = \frac{3}{2} \left( \frac{1}{T_1T} \right)_{\parallel c} = \frac{\mu_0^2 \gamma_n^2 e^2 k_B}{(4\pi)^2} \times \int_{|E| > \Delta} dE \left[ -\frac{\partial f(\varepsilon)}{\partial \varepsilon} \right] \frac{\sqrt{\varepsilon^2 - \Delta^2}}{\hbar^2 c v_F} \ln \frac{2(\varepsilon^2 - \Delta^2)}{\hbar \omega_0 |\varepsilon|}, \quad (6)$$

with  $\varepsilon = \pm \sqrt{v_F^2 k^2 + \Delta^2}$  and  $c$  the distance between nearest neighbor layers. In addition,  $f(\varepsilon)$  is the Fermi function and  $E_g = 2\Delta$  is the gap. In the low- $T$  limit assuming  $\Delta$  is small, this readily evaluates to  $\frac{(\mu_0 \gamma_n e)^2}{(4\pi)^2} \frac{k_B \mu}{\hbar^2 c v_F} \ln(\frac{2\mu}{\hbar \omega_0})$ . Comparing to the result [25] for a 3D point node in the same limits,  $\frac{8\pi}{3} \frac{(\mu_0 \gamma_n e)^2}{(4\pi)^2} \frac{k_B \mu^2}{\hbar^3 v_F^2} \ln(\frac{2\mu}{\hbar \omega_0})$ ,  $1/T_1T$  for the quasi-2D case is the same as the 3D case multiplied by a factor  $\frac{3}{8\pi} \frac{\hbar v_F}{\mu c}$ . Taking  $\mu = 10$  meV,  $v_F = 0.67 \times 10^6$  m/s, and  $c = 6.7 \text{ \AA}$  corresponding to  $\text{ZrTe}_2$ , this is a factor of 7, with the quasi-2D situation enhanced essentially because of the increased phase space for the scattering phenomena leading to Eq. (6), which can include events with  $\Delta k$  covering the entire Brillouin zone in the direction perpendicular to the layers. With the low- $T$   $(1/T_1T)_{\perp c}$  larger by a factor of about 10 as compared to that of the comparable point-node material  $\text{ZrTe}_5$  [9], this indeed makes it plausible that the extended-orbital mechanism for high-mobility Dirac electrons is the dominant mechanism at low temperatures. In the low- $T$  limit, the ratio  $(1/T_1T)_{\perp c}/(1/T_1T)_{\parallel c}$  is smaller than the expected 3/2 given by this model; however, note that Eq. (6) was derived in the low-field limit, and it seems possible that such effects might renormalize the  $(1/T_1T)_{\parallel c}$  results. In addition, while the normal-electron pocket at M is strongly dominated by Zr  $d$ -orbitals; however, a nonzero contribution due to Te states might also lead to a slowly varying background contribution to  $1/T_1T$ .

As shown in Fig. 5(b), we determined that the Dirac spins can give a considerable contribution to Knight shift due to core polarization combined with Landau level splitting for  $B \parallel c$ . However, we expect the corresponding mechanism to give a rather negligible contribution to  $1/T_1T$ . This can be seen from the Korringa relation [29] which can provide an approximate upper limit for the spin  $1/T_1T$ . Note also that in the low- $T$  limit where the Dirac spins are heavily polarized, the probability of spin-flip scattering can be reduced, limiting  $1/T_1T$ . For  $^{125}\text{Te}$ , the Korringa relation will be,  $(1/T_1T)_{\text{spin}} = K_{\text{spin}}^2/[2.6 \times 10^{-6} (\text{s K})^{-1}]$ , and with  $|K_{\text{spin}}|$  at low temperatures determined to be somewhat less than 100 ppm, choosing 100 ppm yields a limiting value  $(1/T_1T)_{\text{spin}} = 4 \times 10^{-3} (\text{s K})^{-1}$ . This is considerably smaller than what is observed. However, the orbital  $1/T_1T$  due to extended high-mobility electrons, described above, is not connected to the shift via a Korringa relation, and from these considerations we determine that the spin-lattice relaxation rate of  $\text{ZrTe}_2$  is dominated by

the orbital contribution. These results will extend across the whole temperature range.

As the temperature increases past 10 K,  $(1/T_1T)_{\parallel c}$  drops rather suddenly, reaching a minimum at about 40 K. This also coincides with a reported drop in the Dirac-carrier mobility, before the high- $T$  regime sets in with different behavior [22]. We believe that the change in  $(1/T_1T)_{\parallel c}$  can be understood in terms of carrier scattering effectively reducing the dimensionality of the relaxation mechanism. Ref. [36] shows that the orbital  $1/T_1T$  process due to high-mobility electrons, which relies upon a logarithmic divergence in the hyperfine coupling mechanism at large distances, will begin to cut off at a distance corresponding to the mean free path ( $\ell$ ) as the scattering rate increases, so that  $1/T_1T$  becomes proportional to  $\ln(\ell)$ . With little or no dispersion for the nodal-line carriers in the direction perpendicular to the layers, the mean free path will certainly be highly anisotropic. Once this length becomes considerably reduced,  $1/T_1T$  will go over to the 2D case, for which  $(1/T_1T)_{\perp c}$  is unchanged but  $(1/T_1T)_{\parallel c}$  will vanish [25, 37]. This is not to say that the layers become completely decoupled; a large reduction in mean free path is sufficient for this change to occur.

Above the minimum,  $(1/T_1T)_{\parallel c}$  again starts to increase vs  $T$ . As seen in the inset of Fig. 5(b), the increase in  $T$  is also accompanied by a drop in chemical potential, as required to maintain charge balance given the large contribution due to  $g_{CB}(\varepsilon)$ . As shown in Figs. 4(a) and (b), there is a split-off band at  $\Gamma$  just below the Dirac node, which is more strongly dominated by Te  $p$ -electrons than the states near the node. With the drop in chemical potential, holes will begin to appear in these states, with a significant effect on the  $^{125}\text{Te}$  NMR because of the orbital weight of these states. There is also a change of character for the  $T$ -dependence of the  $^{125}\text{Te}$  NMR shift, with a small increase in shift appearing for  $B \perp c$ . This behavior matches the observed change in magnetotransport behavior at these temperatures [22], which we believe is a Lifshitz transition corresponding to the chemical potential meeting this split-off band edge. To understand the increase in  $(1/T_1T)_{\parallel c}$  at high temperatures, we show in the Appendix that in addition to the high-mobility electron contribution, the local orbital contribution [36] to  $1/T_1T$ , which does not rely on logarithmic divergence at extended distances, will be larger for the  $B \parallel c$  orientation as long as the Te  $p_z$  contribution exceeds the Te  $p_x$  and  $p_y$  contributions [Fig. 5(c)], which seems to be the case here.

## V. CONCLUSIONS

In conclusion, the topological nature of transition metal dichalcogenide  $\text{ZrTe}_2$  is revealed here as a quasi-2D Dirac semimetal with a nodal line between  $\Gamma$  and  $\text{A}$ . For magnetic fields perpendicular to the  $\text{ZrTe}_2$  layers, the measured shift can be well-modeled by a combination of

orbital shift and spin shift due to high mobility Dirac carriers. We also show that the low-temperature behavior of the spin-lattice relaxation rate can be explained through a quasi-2D Dirac electron model. In the intermediate temperature range, an increase in scattering of the Dirac carriers is applied to interpret the observed fast drop of the spin-lattice relaxation rate for the  $B \parallel c$  orientation. With temperature further increasing, the local orbital contribution starts to dominate the spin-lattice relaxation rate with the significant contribution of a split-off band.

## ACKNOWLEDGMENTS

This work was supported by the Robert A. Welch Foundation, Grant No. A-1526 and Texas A&M University.

## Appendix: Spin-lattice relaxation due to orbital and dipolar interactions

The local orbital contribution to  $1/T_1T$  is the mechanism typically associated with orbital hyperfine coupling in normal metals. As opposed to the extended-orbital mechanism discussed above [35, 36], the local contribution is expected to be limited to orbitals belonging to the atom containing the nucleus being measured. Following the treatment of Obata [38], here we extend the calculation of  $1/T_1T$  to  $p$ -electrons in the tetragonal symmetry corresponding to the 3-fold uniaxial symmetry for Te sites in  $\text{ZrTe}_2$ .

In the tight-binding approximation, the Bloch eigenfunctions are built up from localized atomic functions. For  $p$ -electrons, there are three independent orbital functions  $p_x$ ,  $p_y$  and  $p_z$ . With magnetic field  $B$  along a certain direction, in our case  $x$  and  $z$ , here are the mixed wavefunctions for uniaxial symmetry (omitting the product spin states):

$$\Psi = \begin{cases} \alpha^{1/2} p_z + (1 - \alpha)^{1/2} \frac{1}{\sqrt{2}} (p_x + p_y), & B \parallel c \\ \alpha^{1/2} p_y + (1 - \alpha)^{1/2} \frac{1}{\sqrt{2}} (p_z + p_x), & B \perp c \end{cases} \quad (\text{A.1})$$

where  $\alpha$  is a parameter specifying the relative amount of  $E$  symmetry ( $p_x$  and  $p_y$ ) vs  $A_1$  symmetry ( $p_z$ ) for magnetic field along  $z$  (similarly for  $B \perp c$  with  $\Psi$  rotating correspondingly). For  $B \parallel c$ , when  $\alpha = 0$ , the wavefunction contains only  $p_x$  and  $p_y$ . With  $\alpha = 1$ , only  $p_z$  remains. For both dipolar interaction and orbital interaction contributions, we can thus determine the expressions of the corresponding spin-lattice relaxation rates, starting with a golden-rule relation, for which  $1/T_1 = 2W = 4\pi/\hbar k_B T \langle |\Psi| \mathcal{H} | \Psi \rangle |^2 g^2(\varepsilon_F)$ , where  $\mathcal{H}$  is the orbital or dipolar hyperfine interaction Hamiltonian [38], both of which are proportional to  $1/r^3$  allowing the

relative magnitudes to be readily compared. Also  $g(\varepsilon_F)$  denotes the partial density of states at  $\varepsilon_F$  for the Te  $p$ -orbitals, which are assumed to appear in the relevant band according to the amplitudes given in Eq. (A.1). We obtain the following for the case for dipolar interaction:

$$W_{\text{dip}} = \frac{4\pi}{5} C \left( \left| \int_0^{2\pi} \int_0^\pi \Psi \Psi^* \frac{1}{2} Y_2^0 \sin \theta d\theta d\phi \right|^2 + \left| \int_0^{2\pi} \int_0^\pi \Psi \Psi^* \frac{\sqrt{3}}{2} Y_2^{-1} \sin \theta d\theta d\phi \right|^2 + \left| \int_0^{2\pi} \int_0^\pi \Psi \Psi^* \sqrt{\frac{3}{2}} Y_2^{-2} \sin \theta d\theta d\phi \right|^2 \right) \quad (\text{A.2})$$

$$= \begin{cases} \frac{C}{50} (9\alpha^2 - 12\alpha + 5) & (B \parallel c) \\ \frac{C}{200} (9\alpha^2 + 6\alpha + 5) & (B \perp c), \end{cases}$$

where  $\Psi$  is the wavefunction from Eq. (A.1). Here  $C = 2\pi(\gamma_e \gamma_n \hbar^{3/2})^2 g^2(\varepsilon_F) k_B T \langle r^{-3} \rangle^2$ , where  $\langle r^{-3} \rangle$  comes

from the radial parts of the integrations which are not displayed in Eq. (A.2). The integrals can be analytically evaluated giving the results also shown in Eq. (A.2). For the case of the orbital interaction, the corresponding relations are

$$W_{\text{orb}} = \frac{C}{2} |\langle \Psi | l^{-1} | \Psi \rangle|^2$$

$$= \begin{cases} 2C\alpha(1 - \alpha) & (B \parallel c) \\ \frac{C}{2}(1 - \alpha^2) & (B \perp c). \end{cases} \quad (\text{A.3})$$

These results are shown in Fig. 5(c) in the main text. As anticipated [38] the orbital term dominates in almost all cases. Also there is a crossing of thermals at  $\alpha = 1/3$  which represents an equal mixture of orbitals, as expected since such a mixture becomes isotropic. When  $\alpha$  is larger than  $1/3$ , the local orbital contribution for  $B \parallel c$  exceeds that for  $B \perp c$ .

---

[1] S. Manzeli, D. Ovchinnikov, D. Pasquier, O. V. Yazyev, and A. Kis, *Nat. Rev. Mater.* **2**, 17033 (2017).

[2] A. J. S. Machado, N. P. Baptista, B. S. De Lima, N. Chaia, T. W. Grant, L. E. Corrêa, S. T. Renosto, A. C. Scaramussa, R. F. Jardim, M. S. Torikachvili, et al., *Phys. Rev. B* **95**, 144505 (2017).

[3] P. Tsipas, D. Tsoutsou, S. Fragkos, R. Sant, C. Alvarez, H. Okuno, G. Renaud, R. Alcotte, T. Baron, and A. Dimoulas, *ACS Nano* **12**, 1696 (2018).

[4] I. Kar, J. Chatterjee, L. Harnagea, Y. Kushnirenko, A. V. Fedorov, D. Shrivastava, B. Büchner, P. Mahadevan, and S. Thirupathaiah, *Phys. Rev. B* **101**, 165122 (2020).

[5] Q. Li, D. E. Kharzeev, C. Zhang, Y. Huang, I. Pletikosić, A. V. Fedorov, R. D. Zhong, J. A. Schneeloch, G. D. Gu, and T. Valla, *Nat. Phys.* **12**, 550 (2016).

[6] F. Tang, Y. Ren, P. Wang, R. Zhong, J. Schneeloch, S. A. Yang, K. Yang, P. A. Lee, G. Gu, Z. Qiao, et al., *Nature* **569**, 537 (2019).

[7] G. Manzoni, L. Gragnaniello, G. Autès, T. Kuhn, A. Sterzi, F. Cilento, M. Zachigna, V. Enenkel, I. Vobornik, L. Barba, et al., *Phys. Rev. Lett.* **117**, 237601 (2016).

[8] Z. Fan, Q.-F. Liang, Y. B. Chen, S.-H. Yao, and J. Zhou, *Sci. Rep.* **7**, 45667 (2017).

[9] Y. Tian, N. Ghassemi, and J. H. Ross, Jr., *Phys. Rev. B* **100**, 165149 (2019).

[10] S. Takahashi, T. Sambongi, J. W. Brill, and W. Roark, *Solid State Commun.* **49**, 1031 (1984).

[11] Z. Zhu, G. W. Winkler, Q. Wu, J. Li, and A. A. Soluyanov, *Phys. Rev. X* **6**, 031003 (2016).

[12] A. H. Reshak and S. Auluck, *Physica B* **353**, 230 (2004).

[13] H. Guo, N. Lu, L. Wang, X. Wu, and X. C. Zeng, *J. Phys. Chem. C* **118**, 7242 (2014).

[14] Z. Muhammad, B. Zhang, H. Lv, H. Shan, Z. u. Rehman, S. Chen, Z. Sun, X. Wu, A. Zhao, and L. Song, *ACS Nano* **14**, 835 (2019).

[15] M. Inamo, *Chem. Lett.* **25**, 17 (1996).

[16] G. K. H. Madsen, P. Blaha, K. Schwarz, E. Sjöstedt, and L. Nordström, *Phys. Rev. B* **64**, 195134 (2001).

[17] J. P. Perdew, K. Burke, and M. Ernzerhof, *Phys. Rev. Lett.* **77**, 3865 (1996).

[18] P. Blaha, K. Schwarz, F. Tran, R. Laskowski, G. K. H. Madsen, and L. D. Marks, *J. Chem. Phys.* **152**, 074101 (2020).

[19] H. J. Monkhorst and J. D. Pack, *Phys. Rev. B* **13**, 5188 (1976).

[20] I. Orion, J. Rocha, S. Jobic, V. Abadie, R. Brec, C. Fernandez, and J.-P. Amoureaux, *Dalton Trans.* **20**, 3741 (1997).

[21] H. Weng, X. Dai, and Z. Fang, *Phys. Rev. X* **4**, 011002 (2014).

[22] H. Wang, C. H. Chan, C. H. Suen, S. P. Lau, and J.-Y. Dai, *ACS Nano* **13**, 6008 (2019).

[23] N. P. Armitage, E. J. Mele, and A. Vishwanath, *Rev. Mod. Phys.* **90**, 015001 (2018).

[24] Z. Okvátovy, H. Yasuoka, M. Baenitz, F. Simon, and B. Dóra, *Phys. Rev. B* **99**, 115107 (2019).

[25] H. Maebashi, T. Hiroawa, M. Ogata, and H. Fukuyama, *J. Phys. Chem. Solids* **128**, 138 (2019).

[26] Z. Li, L. Chen, S. Meng, L. Guo, J. Huang, Y. Liu, W. Wang, and X. Chen, *Phys. Rev. B* **91**, 094429 (2015).

[27] G. Mikitik and Y. V. Sharlai, *Phys. Rev. B* **101**, 205111 (2020).

[28] S. Xu, C. Bao, P.-J. Guo, Y.-Y. Wang, Q.-H. Yu, L.-L. Sun, Y. Su, K. Liu, Z.-Y. Lu, S. Zhou, et al., *Nat. Commun.* **11**, 1 (2020).

[29] G. C. Carter, L. H. Bennett, and D. J. Kahan, *Metallic shifts in NMR: a review of the theory and comprehensive critical data compilation of metallic materials* (Pergamon, New York, 1977).

[30] S. Jeon, B. B. Zhou, A. Gyenis, B. E. Feldman, I. Kimchi, A. C. Potter, Q. D. Gibson, R. J. Cava, A. Vishwanath, and A. Yazdani, *Nat. Mater.* **13**, 851 (2014).

[31] Y.-S. Fu, T. Hanaguri, K. Igarashi, M. Kawamura, M. S.

Bahramy, and T. Sasagawa, *Nat. Commun.* **7**, 1 (2016).

[32] Y. Liu, X. Yuan, C. Zhang, Z. Jin, A. Narayan, C. Luo, Z. Chen, L. Yang, J. Zou, X. Wu, et al., *Nat. Commun.* **7**, 1 (2016).

[33] J. Hu, Z. Tang, J. Liu, Y. Zhu, J. Wei, and Z. Mao, *Phys. Rev. B* **96**, 045127 (2017).

[34] C. P. Slichter, *Principles of Magnetic Resonance* (Springer, New York, 1990).

[35] P. Lee and N. Nagaosa, *Phys. Rev. B* **43**, 1223 (1991).

[36] A. Knigavko, B. Mitrović, and K. V. Samokhin, *Phys. Rev. B* **75**, 134506 (2007).

[37] B. Dóra and F. Simon, *Phys. Rev. Lett.* **102**, 197602 (2009).

[38] Y. Obata, *J. Phys. Soc. Jpn.* **18**, 1020 (1963).